Extrapolation of the astrophysical S factor for $^7\mathrm{Be}(p,\gamma)^8\mathrm{B}$ to solar energies

B. K. Jennings, S. Karataglidis, and T. D. Shoppa

TRIUMF, 4004 Wesbrook Mall, Vancouver, British Columbia, Canada V6T 2A3

(Received 23 June 1998)

We investigate the energy dependence of the astrophysical S factor for the reaction $^7\mathrm{Be}(p,\gamma)^8\mathrm{B}$, the primary source of high-energy solar neutrinos in the solar pp chain. Using simple models we explore the model dependence in the extrapolation of the experimental data to the region of astrophysical interest near 20 keV. We find that below approximately 400 keV the energy dependence is very well understood and constrained by the data for the elastic scattering of low-energy neutrons from $^7\mathrm{Li}$. Above 400 keV nuclear distortion of the wave function of the incident proton introduces a significant model dependence. This is particularly important for the s-wave contribution to the S factor. The extracted value of $S(0)$ is $19.0 \pm 1.0 \pm 0.2$ eV b. The first error is experimental while the second is an estimate of the theoretical error in the extrapolation.
[S0556-2813(98)01812-3]

PACS number(s): 26.65.+t, 25.60.Pj, 25.40.Lw, 24.50.+g

I. INTRODUCTION

The $^7\mathrm{Be}(p,\gamma)^8\mathrm{B}$ reaction, at energies of approximately 20 keV, plays an important role in the production of solar neutrinos [1]. The subsequent decay of the $^8\mathrm{B}$ is the source of the high-energy neutrinos to which many solar neutrino detectors are sensitive. The cross section for this reaction is conventionally expressed in terms of the S factor which is defined in terms of the cross section σ by

$$S(E) = \sigma(E)E\, \exp[2\pi\eta(E)], \tag{1}$$

where $\eta(E) = Z_1 Z_2 \alpha \sqrt{\mu c^2/2E}$ is the Sommerfeld parameter, α is the fine structure constant, and μ is the reduced mass. The definition of the S factor eliminates from it most of the energy dependence due to Coulomb repulsion by factoring out the penetration to the origin of a particle in the Coulomb potential of a point charge. However, it does not make the S factor energy independent, as there are still energy dependences due to the structure of the final bound state, resonances, and the attenuation of the barrier by the nuclear mean field. The reaction rate, obtained by folding the thermal distribution of nuclei in the stellar core with the cross section, peaks at approximately 20 keV. Because the cross section diminishes exponentially at low energies, the only method of obtaining information about the S factor at energies of astrophysical interest is to extrapolate data taken at experimentally accessible energies ($E > 100$ keV). To do the extrapolation reliably we must understand the physics associated with the S factor.

To illustrate the problem of extrapolating the data to astrophysical energies we show in Fig. 1 a fit to the experimental data [2–4] that uses just a straight line and a fit with a calculation that includes s-wave nuclear distortion through a hard sphere potential of radius 4.1 fm. The straight line and potential model fits are displayed by a solid and dashed line, respectively. The latter calculation will be described in more detail in Sec. III. In both cases a Breit-Wigner resonance is included. As can be seen from the figure both fits to the data are equally good; $\chi^2 = 0.9$ in each case. However, there is a marked difference in the S factors at 20 keV: 15.3 and 21.0

eV b for the straight line fit and the hard sphere model, respectively, a 37% variation in the extrapolated value. Such a large difference must be understood if reliable extrapolations are to be made and a variety of, sometimes conflicting, models [5–15] have been developed for this purpose.

The dashed curve in Fig. 1 shows an upturn in the S factor at threshold. This is a feature common to all of the model calculations of the astrophysical S factor for the $^7\mathrm{Be}(p,\gamma)^8\mathrm{B}$ reaction (with the exception of the straight line fit). It has been established [15] that this behavior stems from a pole in the S factor when the photon energy E_γ vanishes.

We develop two key concepts for the description of the astrophysical S factor: the pole where the photon energy vanishes and an effective hard sphere radius. These concepts will be developed and explored by modeling the complicated multidimensional many-body system with simple one-body models. The pole term describes and is dominated by Coulomb physics. It depends on nuclear physics through the separation energy, the asymptotic normalization of the final
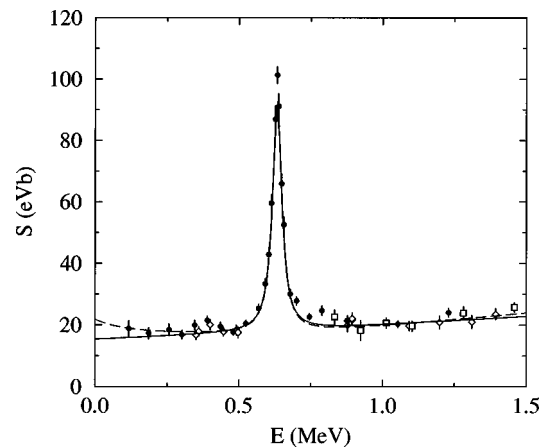

FIG. 1. Different fits to the experimental S-factor data. The solid curve is a straight line plus the resonance while the dashed curve is a calculation with a hard sphere cutoff radius of 4.1 fm plus the resonance. $\chi^2 = 0.9$ in both cases. The data are from Vaughn *et al.* [3] (squares), Filippone *et al.* [2] (circles), and Hammache *et al.* [4] (diamonds).

state wave function, and the spectroscopic factors. The separation energy of the valence proton from ^8B is 137.5 keV [16] and determines the pole location. The asymptotic normalization and the spectroscopic factor combine in an asymptotic strength parameter, defined in Sec. II, to give the residue of the pole. This will be determined by a fit to the S-factor data. An effective hard sphere repulsion is introduced to approximate how the nuclear physics influences the energy dependence, and is related primarily to the nonresonant phase shift of the initial scattering state. The effective hard sphere radius is determined by comparing the hard sphere model to more complete models such as potential models. Elastic scattering data from protons on ^7Be, if it existed, would help constrain the potential models and through them the effective hard sphere radius. As such data are presently unavailable, the constraints must come from the elastic scattering of neutrons from ^7Li, the mirror system. The concepts of the pole and the hard sphere repulsion lead to a simple rational approximation for the energy dependence of the S factor, which encompasses the dominant physics at low energy.

This simple approach breaks down as the energy increases and the capture becomes more sensitive to the internal structure of the ^7Be core. We explore the range of validity of the simple one-dimensional model by comparing it with more sophisticated potential, R-matrix, and microscopic cluster models. In general, the simple approach agrees with the potential and R-matrix models over a larger energy range. Alternatively, within its range of validity, we may use the hard sphere model based on an effective hard sphere radius and Coulomb physics to understand and critique other models.

We present a brief review of the formalism in Sec. II and show how the pole in the S factor arises. In Sec. III the hard sphere model is presented and used to derive a simple expression for the energy dependence of the S factor. The hard sphere model is compared to the cluster model calculations in Sec. IV. In Sec. V we use the final arbiter, the experimental data, to discriminate between the models and determine which is best for the extrapolation. In Sec. VI we present our best estimates for the S factor near threshold and draw some conclusions.

II. POLE TERM

Most calculations of the S factor follow the pioneering work of Christy and Duck [5] to which we refer the reader for more details. Here we present a brief overview of the model. The E1 contribution to the S factor for the $^7Be(p,\gamma)^8B$ reaction may be written as

$$S = C(I_0^2 + 2I_2^2)E_\gamma^3(J_{11}\beta_{11}^2 + J_{12}\beta_{12}^2)\frac{1}{1-e^{-2\pi\eta}}, \quad (2)$$

where

$$I_l = \int_0^\infty r^2 dr r \psi_{il}(r)\psi_f(r), \quad (3)$$

$$C = \frac{5\pi}{9}\frac{1}{(\hbar c)^3}(2\pi\eta k)e^2\mu^2\left(\frac{Z_1}{M_1} - \frac{Z_2}{M_2}\right)^2. \quad (4)$$

In Eq. (2), J_{LS} is the spectroscopic factor for a given angular momentum L and channel spin S, β_{LS} is the asymptotic normalization of the bound state wave function, E_γ is the photon energy, and k is the momentum of the incident proton. The extra factor of r in the integrand comes from the photon wave function. The final bound state wave function $\psi_f(r)$ is normalized in the asymptotic region to $\psi_f(r) = W_{\alpha,l}(\kappa r)/r$ while the initial wave function reduces to the regular Coulomb wave function divided by $kr\sqrt{2\pi\eta}/(e^{2\pi\eta}-1)$. The unusual choice of normalizations is just to simplify the mathematics and generate integrals that are well behaved at threshold. The initial state has both Coulomb and nuclear distortions. The Coulomb distortions are large and give the penetration factor included in the definition of the S factor, Eq. (1). They are included in all calculations. The nuclear distortions are much smaller but they are important and introduce a significant model dependence into the calculations, as described in the next section.

The absolute magnitude of the S factor is determined primarily by the spectroscopic factor and the asymptotic normalization (see also Ref. [17]). The spectroscopic factor contains many-body aspects of the problem and is calculable from standard shell model theory. The asymptotic normalization also depends on the many-body wave function, but is far more difficult to estimate from first principles: it requires detailed knowledge of how the eight-body wave function extends beyond the nuclear potential and its mapping to the Whittaker function in this region. This may be estimated crudely by approximating that behavior by using a suitably chosen Woods-Saxon wave function for the weakly bound proton. Instead we treat the overall factor $A_n = J_{11}\beta_{11}^2 + J_{12}\beta_{12}^2$ as a free parameter, which is independent of energy and determined by the S-factor data. For simplicity we will refer to this combination of asymptotic normalization and spectroscopic factor as the asymptotic strength.

To investigate the behavior of the integrals in Eq. (2), we first consider $\psi_f(r) = W_{\alpha,l}(\kappa r)/r$ for all radii and take $\psi_{i0}(r) = F_0(kr)/\{kr\sqrt{2\pi\eta}/(e^{2\pi\eta}-1)\}$. The s-wave integral then becomes

$$I_0 = \int_0^\infty dr r \frac{W_{\alpha,l}(kr)F_0(kr)}{k\sqrt{2\pi\eta}}(e^{2\pi\eta}-1). \quad (5)$$

The integral is smooth as k passes through zero and diverges as $k \to i\kappa$ $(E \to -E_B)$. The nature of the divergence is determined by the asymptotic forms of the Coulomb wave function and Whittaker function for large r. There the Whittaker function is proportional to $r^{-|\eta k|/\kappa}e^{-\kappa r}$ [5] (ηk is independent of k). Above threshold the Coulomb wave function oscillates at large radii; however, below threshold it is exponentially growing and is proportional to $r^{|\eta|}e^{|k|r}$. Thus the behavior of the integrand at large radius is

$$r^{1-|\eta k|(1/\kappa - 1/|k|)}\exp[-(\kappa - |k|)r] \quad (6)$$

and the integral diverges as

$$I_0 \sim 1/(\kappa - |k|)^2 \sim 1/(E_B + E)^2 = 1/E_\gamma^2. \quad (7)$$

The S factor is proportional to $I_0^2 E_\gamma^3$, and gives rise to a simple pole in S at $E_\gamma = 0$. However, the first correction term
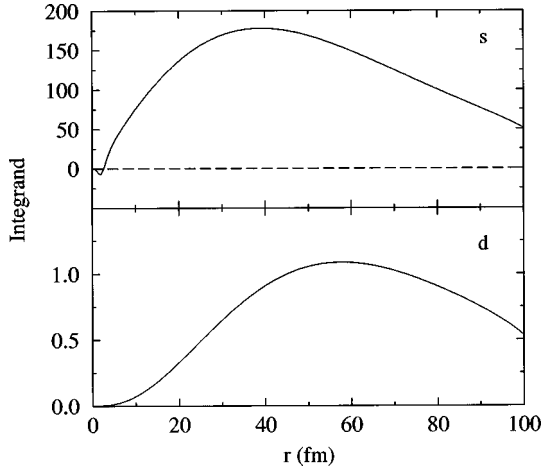
FIG. 2. The integrand for the *s*-wave and *d*-wave contributions to the *S* factor at 0.0 MeV. The calculations were done with a Woods-Saxon potential.

FIG. 3. The integrand for the *s*- and *d*-wave contributions to the *S* factor at 0.0 MeV, 0.5 MeV, and 1.5 MeV. The solid line is a full calculation with a Woods-Saxon potential. The dot-dashed line has no nuclear distortion of the incoming wave and uses a Whittaker function for the bound state. The dashed curve is the extrapolation of full calculation to short distance using only the Coulomb potential.

is not simply $1/E_\gamma$ but rather of the form $(1+c \ln E_\gamma)/E_\gamma$, the logarithmic term coming from the $r^{-|\eta k|(1/\kappa-1/|k|)}$ factor. Both the leading and first correction terms are determined purely by the asymptotic behavior of the wave functions. The second correction term, of order E_γ^0, is not determined purely by the asymptotic value of wave function alone but also depends on the wave function at finite r.

The presence of the pole suggests the *S* factor may be parametrized as a Laurent series:

$$S = d_{-1}E_\gamma^{-1} + d_0 + d_1 E_\gamma + \cdots. \tag{8}$$

The coefficients of the first two terms, d_{-1} and d_0, are determined purely by the asymptotic forms of the wave functions while the third coefficient d_1 is also dependent on the short-range properties of the wave functions. The validity of such an approximation is discussed below.

III. ONE-BODY MODELS AND RATIONAL APPROXIMATIONS

The energy dependence in the *S* factor enters through the *s*- and *d*-wave integrals I_0 and I_2 and the phase-space factor E_γ^3. To investigate that behavior, we present in Fig. 2 the integrands, Eq. (3), for both the *s* and *d* waves. A Woods-Saxon potential model, denoted B1, whose radius (2.39 fm) and diffuseness (0.65 fm) were taken from Barker [7], was used to calculate the bound state and nuclear distortions. A potential depth of -46.6 MeV was chosen to reproduce the binding energy of the final state. No spin-orbit force was included. The integrands are peaked at very large radii, 40 fm and 55 fm for the *s*- and *d*-wave integrands, respectively, and extend well beyond 100 fm. As this is well outside the range of the nuclear potential ($r_{rms}=2.48\pm0.03$ fm for ^{7}Be [18]), the capture is purely Coulombic. To ensure complete convergence in our calculations we integrated to 1000 fm. The small negative contribution and the node in the *s*-wave integral near 0 fm arise from the effects of the nuclear distortion. The distortion in the *d*-wave component is negligible.
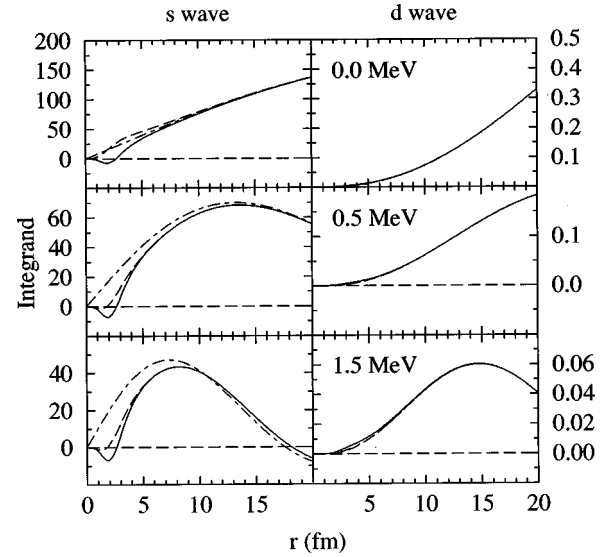
We show the integrands for a range of energies in Fig. 3.

The peaks in the integrands, which are displayed by the solid lines, are outside the range of the nuclear force even at 1.5 MeV. Two other calculations, in which the nuclear distortion is varied, are also presented. The pure Coulomb calculation, Eq. (5), contains no nuclear distortions and is displayed by the dot-dashed line. The other curve (dashed line) matches the full calculation at large distances, and so it has the same nuclear phase shift at large radii, but the initial wave function is integrated to small radii using just the Coulomb potential. In the *s*-wave integrands the nuclear distortions play an important role, especially near the origin. These distortions produce a node in the scattering wave function and give a repulsive phase shift. The node is necessary to make the scattering wave function orthogonal to the bound $0s$-shell protons in the ^{7}Be core. That orthogonality is preserved only if the node in the scattering state is at a radius where the bound state wave function is still appreciable. Hence the node will be close to but inside the nuclear radius. There are no bound $0d$-shell protons in ^{7}Be and hence no node in the *d*-wave integrand. Consequently the *d*-wave phase shift is small and attractive.

The integrals corresponding to the integrands plotted in Fig. 3 are given in Table I. The largest change in the *s*-wave integral comes from the nuclear phase shift at large radii, as is evident when partial nuclear distortion is introduced. The additional distortion coming from the short-range nuclear potential produces a smaller but still significant change in the integral. This is common to the integrals evaluated at 0.5 and 1.5 MeV. In the case of the *d*-wave integral, the total effect of nuclear distortions is quite small, at most 2%, even at 1.5 MeV.

Since the *S* factor is sensitive to the phase shift, the potential should reproduce the nuclear phase shifts. Unfortunately, there are no experimental data for the scattering of protons from ^{7}Be from which the phase shifts may be deter-

TABLE I. The effects of nuclear distortion on the direct capture matrix elements using a Woods-Saxon potential. The calculations are as discussed in the text.

Model	s-wave		d-wave	
energy	0.5 MeV	1.5 MeV	0.5 MeV	1.5 MeV
Full distortion	517.5	115.6	241.1	95.12
Partial distortion	525.2	121.8	242.2	97.59
No distortion	550.7	135.1	240.7	93.58
Pure Coulomb	560.4	144.5	240.8	93.77

mined. However, data are available for the scattering in the mirror system, ^{7}Li-n, for which we follow Barker's analysis [7] to determine the potential depths. From the elastic scattering of thermal neutrons from ^{7}Li, the scattering lengths are $a_1 = 0.87 \pm 0.07$ fm and $a_2 = -3.63 \pm 0.05$ fm [19], where a_S is the scattering length for the channel spin S. The depths of the potentials are adjusted to fit these scattering lengths, giving -46.58 MeV and -56.21 MeV for the $S=1$ and 2 potentials, respectively. The $S=1$ potential depth is very similar to the one we have used for the first Woods-Saxon potential model but the $S=2$ potential is significantly stronger. These nuclear potentials are then used in the calculation of the S factor for ^{7}Be(p,γ). This assumes isospin symmetry for the nuclear mean field. The contributions for the two channel spins are combined using Barker's spectroscopic factors [7]. We refer to this potential model as B2.

In Fig. 3, we see that the s-wave nuclear distortion is dominated by the node in the scattering state wave function. This suggests that we may construct a simple model, the hard sphere model discussed in the Introduction, where the initial state wave function is zero inside some radius r_c and a pure Coulomb wave outside. We impose the boundary condition that the wave function be zero at r_c. This generates a phase shift and is equivalent to having an infinitely repulsive potential with a radius r_c. The d-wave scattering state is taken to be an undistorted Coulomb wave function. The bound state is assumed to be a pure Coulomb state, described by a Whittaker function, for all radii.

We saw for the potential model that it was necessary to have different potential depths for different channel spins. For the hard sphere model this would suggest that we use different cutoff radii for different channel spins. However, the simple model does not justify such elaborations and we find that with just a single, suitably chosen, radius we can reproduce the low-energy results from a given potential model. The use of a single radius does, however, weaken the connection between the hard sphere radius and the elastic scattering phase shift. We make the connection only through the intermediary of the potential model.

The S factors from the hard sphere model are compared to the S factor of other one-body models in Fig. 4. In Fig. 4(a), the solid curve is the result of the hard sphere model, with $r_c = 2.4$ fm, while the dashed curve displays the result of the Woods-Saxon potential, B1. The curves have been normalized to agree at $E = 100$ keV. There is remarkable agreement between the two results up to 1.5 MeV, suggesting that the hard sphere model encapsulates the physics of the Woods-Saxon potential model. In Fig. 4(b) we show the results of a hard sphere model calculation with radius $r_c = 1.0$ fm, the
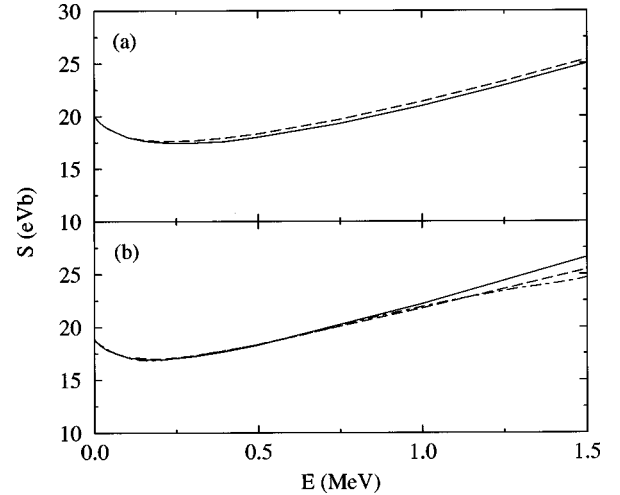

FIG. 4. The S factor as a function of energy for different one-body models. All curves are normalized to the same value at 0.1 MeV. In (a) the solid line is a hard sphere model with $r_c = 2.4$ fm while the dashed line is the B1 Woods-Saxon model. In (b), the model with $r_c = 1.0$ fm, the B2 model, and the R-matrix model of Barker are displayed by the solid, dashed, and dot-dashed lines, respectively.

calculation with the B2 potential, and Barker's R-matrix calculation with $a = 4$ fm [9]. That choice of a is predicated on the result that, in the R-matrix formalism, the matching radius should be roughly the sum of the radius and diffuseness of the potential [20]. The level of agreement is again quite good.

One advantage of the hard sphere model is that it is possible to do an explicit Taylor series expansion about $E = 0$ MeV and obtain directly the derivatives of S at threshold. Following Williams and Koonin [21] we employ the Bessel function expansion [22] of the Coulomb wave functions to generate the Taylor series expansion. Each term involves E-independent radial integrations of Bessel functions, powers, and Whittaker functions. For a hard sphere radius of 2.4 fm the integrations may be done to yield the series

$$S(E)/S(0) = 1 - 1.917E + 15.69E^2 - 110.28E^3$$
$$+ 774.1E^4 + \cdots, \qquad (9)$$

where E is in MeV. The coefficients are increasing in size and alternate in sign. Given the pole in the S factor, the radius of convergence is $E = E_B = 137.5$ keV. We stress that the coefficients in Eq. (9) were not obtained by a fit of the S factor over a finite energy region but rather through an explicit series expansion of the S factor in powers of the energy.

A similar expansion has been used by Baye et al. [23] to obtain the first derivative of the S factor at threshold. They utilize a slightly different Bessel function expansion for the Coulomb functions. It can be obtained from that used by Williams and Koonin [21] by using the recurrence relations for the Bessel functions. For the choice of cutoff radius of Baye et al., 2.0 fm, we reproduce their numerical results.

A more convergent and pedagogically useful expansion may be developed. Motivated by the Laurent series of Eq. (8), the Padé approximant discussion of Ref. [15], and the

TABLE II. The percentage error obtained by using various expansions of the S factor for $r_c = 2.4$ fm. The errors introduced by using a rational approximation [Eq. (11)], a second order Taylor series expansion, a third order Taylor series expansion, and the logarithmic expansion of Ref. [21] are denoted by δS_r, δS_{T2}, δS_{T3}, and δS_W, respectively.

E (MeV)	δS_r (%)	δS_{T2} (%)	δS_{T3} (%)	δS_W (%)
0.00	0.00	0.00	0.00	0.00
0.02	−0.02	0.06	−0.03	0.04
0.10	−0.11	7.22	−5.03	5.34
0.30	−0.36	110.78	−230.92	124.51
0.40	−0.56	211.84	−590.43	384.07
0.50	−1.40	340.70	−1191.88	1259.63
1.00	−6.64	1309.96	−9214.33	1.4×10^7

knowledge that there is a pole at $E_\gamma = 0$ MeV, we Taylor series expand $E_\gamma S$. This removes the effect of the simple pole in the expansion. To recover S we divide by E_γ thus obtaining a rational approximation

$$S(E)/S(0) = \frac{0.1375 + 0.7361E + 0.2392E^2 + \cdots}{0.1375 + E} \quad (10)$$

$$\approx \frac{a}{E_B + E} + b + cE, \quad (11)$$

with $a = 0.0408$ MeV, $b = 0.7033$, and $c = 0.2392$ MeV^{-1}. By construction, $a/E_B + b = 1$. The rational approximation, Eqs. (10) or (11), is very similar to a Padé approximant. The Padé approximant is a ratio of polynomials with all the parameters determined by fitting the derivatives at the expansion point. However, in Eq. (10), the position of the pole is fixed by the binding energy. As a result, for the same order polynomials one fewer derivative is required. The coefficients in the rational approximation, Eq. (10), are growing much more slowly than in the Taylor series expansion, Eq. (9). This is due to the better convergence of the rational approximation. The coefficients do, however, begin to grow more rapidly after the cubic term in the numerator.

The accuracy of the rational approximation [Eq. (11)] is shown in Table II. This approximation is valid to better than 1% up to 400 keV. By comparison, the Taylor series expansion and the logarithmic derivative expansion break down below 100 keV as expected given the radius of convergence. Although all approaches are accurate in the astrophysical region near 20 keV, only the rational approximation is accurate out to the region which is accessible by experiment.

The coefficients a, b, and c in Eq. (11) are given in Table III for a variety of models. In the case of the hard sphere models, the pole and constant terms are the same to within 0.5% while the linear term varies by a factor of almost 6. This confirms that the constant and pole terms are coupled in an almost model-independent manner while the linear term is strongly dependent on initial state nuclear distortions.

The first and second logarithmic derivatives are also given in Table III for comparison with the results of Williams and Koonin [21]. They have a binding energy of 136 keV and use a hard sphere model with $r_c = 4.1$ fm in both the s and d waves. We agree with Barker [8] that this choice of radius is

TABLE III. Coefficients of the expansion Eq. (11). Also shown are the first and second logarithmic derivatives at threshold. The first four rows are for the hard sphere model with different cutoff radii. The fifth row contains the results from Williams and Koonin [21] while the sixth, seventh, and eighth rows are with Woods-Saxon potentials. The last two rows contain values of the derivatives from previous work.

Model	a (MeV)	b	c (MeV^{-1})	$d\ln S/dE$ (MeV^{-1})	$d^2\ln S/dE^2$ (MeV^{-2})
$r_c = 0.0$ fm	0.0409	0.702	0.390	−1.77	28.3
$r_c = 1.0$ fm	0.0409	0.703	0.343	−1.82	28.1
$r_c = 2.4$ fm	0.0408	0.703	0.239	−1.92	27.7
$r_c = 4.1$ fm	0.0407	0.704	0.067	−2.09	27.0
WK [21]	0.0425	0.687	0.050	−2.35	28.3
B1 [7]	0.0420	0.695	0.310	−1.91	28.6
B2 [7]	0.0417	0.697	0.367	−1.84	28.7
T [10]	0.0409	0.703	0.200	−1.96	27.6
Barker [8]	—	—	—	−1.41	10.2
Adelberger et al. [24]	—	—	—	−0.70	3.3

poorly motivated and we find that none of the Woods-Saxon or generator coordinate models considered herein are consistent with a hard sphere model with $r_c > 3$ fm. Williams and Koonin are also missing a factor of 2 for the d-wave term in their Eq. (1).

Also, in Table III, we make the comparison of the parametrization of the hard sphere models to those for three different Woods-Saxon calculations. The parametrization, Eq. (11), for the Woods-Saxon models was determined from fitting the S factor at 0, 20, and 40 keV. For two of the calculations, we use the B1 and B2 models introduced previously. For the third, the radius and diffuseness parameters were obtained from Tombrello [10] while the potential depth was adjusted to reproduce the binding energy of the final state. No spin-orbit force was included. The third calculation is denoted as T. The results for the B1 and T models are quite close to those of the hard sphere model with $r_c = 2.4$ fm. While the a and b coefficients in the B2 model are consistent with those of the other Woods-Saxon models, the linear term c is closer to the hard sphere model with $r_c = 1.0$ fm. This is consistent with the agreement we have seen in Fig. 4 between the B2 model and the hard sphere model with that radius.

Attempts have been made to obtain the derivatives at threshold by a quadratic fit to either S or $\ln S$ over an extended energy range. The derivatives obtained by this method tend to disagree among themselves and with our results. The derivatives from two such fits are shown in the last two rows of Table III. The first is a fit to $\ln S$ by Barker [8] over the energy range 0–100 keV. He uses a Woods-Saxon potential model to obtain S. The second is from Adelberger et al. [24]. There S is obtained from a generator coordinate calculation [6] and fit over the energy range 20–300 keV. As shown in Table II, Taylor series expansions about the origin are not valid over the energy ranges used for the fits. We find that in order to accurately determine both the first and second derivatives at the origin it is necessary to restrict the fit region to less than 10 keV. The Taylor series expansion con-
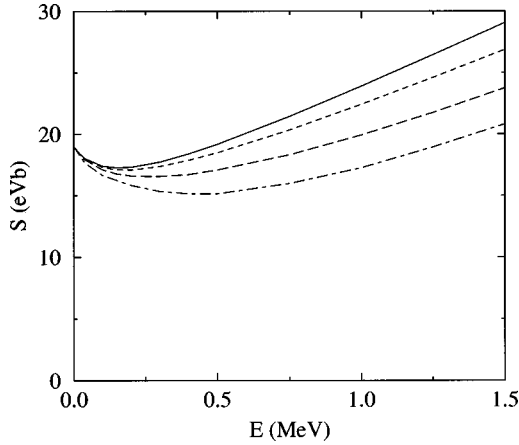
FIG. 5. The S factor as a function of energy for a range of cutoff radii. The results obtained for $r_c = 0.0$, 1.0, 2.4, and 4.1 fm are shown by the solid, short-dashed, long-dashed, and dot-dashed lines, respectively. All the curves are normalized to 19 eV b at threshold.

verges well in this energy region. We can, however, qualitatively reproduce the numbers of Barker and Adelberger $et\ al.$ for the derivatives from our models if we use their fit regions. Thus the differences in the numbers obtained are not primarily from differences in the models but rather due to how the derivatives were obtained. They indicate the sensitivity to the fit range chosen.

While a quadratic form does not work well near threshold it is quite good if that region is excluded. For example, a fit to the S factor over the range 30–300 keV is accurate to better than 0.4% except very near the end points. Using this fit to extrapolate to threshold gives almost a 3% error in $S(0)$, not too surprising given that the quadratic form ignores the existence of the pole at $E = -137.5$ keV.

To further illustrate the role of nuclear distortions, the S factors for the cutoff radii of Table III are shown in Fig. 5. The curves with $r_c = 0.0$, 1.0, 2.4, and 4.1 fm are displayed by the solid, short-dashed, long-dashed, and dot-dashed lines, respectively. All the curves are normalized to 19.0 eV b at threshold. The effect of nuclear distortion is quite noticeable even at energies as low as 100 keV, and increases with increasing energy. Figure 5, together with Fig. 4, highlights an important aspect of the models: the equivalent hard sphere radius is sensitive to the choice of potential depth. Analogously, the phase shift and degree of nuclear distortion are model dependent. The effect of nuclear distortion is also seen in Table IV where the ratios $S(0)/S(20)$,

TABLE IV. The energy dependence of the S factor at low energy for various cutoff radii and Woods-Saxon models.

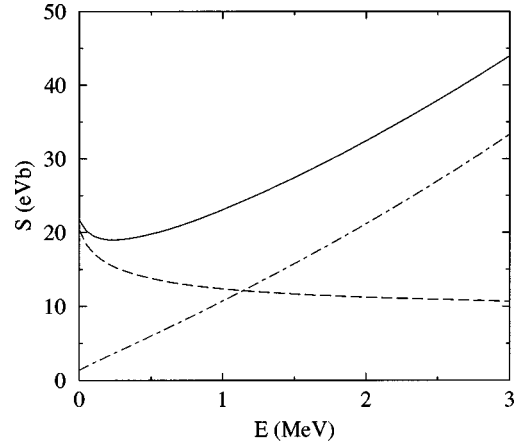| Model	$S(0)/S(20)$	$S(20)/S(100)$	$S(0)/A_n$
$r_c = 0.0$ fm	1.03	1.06	38.2
$r_c = 1.0$ fm	1.03	1.06	38.1
$r_c = 2.4$ fm	1.03	1.07	37.8
$r_c = 4.1$ fm	1.04	1.10	37.2
B1 [7]	1.03	1.08	37.8
B2 [7]	1.03	1.06	38.0
T [10]	1.03	1.08	37.6

FIG. 6. The S factor, as calculated with $r_c = 2.4$ fm. The total result is displayed by the solid line, while the s- and d-wave components are shown by the dashed and dot-dashed lines, respectively.

$S(20)/S(100)$, and $S(0)/A_n$ are given. The variation in the last ratio is almost 3%, indicating that the S factor is sensitive to nuclear distortions even at threshold.

Nunes $et\ al.$ [14] have also calculated the S factor with a Woods-Saxon potential, but used the parametrization of Kim $et\ al.$ [12]. We find good agreement with their calculations and, in particular, concur with their observation of large effects due to nuclear distortions in that particular model. The parametrization of Kim $et\ al.$ generates an S factor with a slightly different energy dependence, corresponding to a hard sphere model with $r_c = 3.0$ fm.

The relative s- and d-wave contributions to the S factor, calculated for $r_c = 2.4$ fm, are displayed in Fig. 6. The total, s-wave, and d-wave parts are displayed by the solid, dashed, and dot-dashed lines, respectively. The upturn at threshold is purely from the s-wave component, even though the s- and d-wave capture leads to the same final state. The linear behavior in the d-wave component is a result of the zero in the Coulomb function which lies very close to the position of the pole. In general, partial waves for nonzero orbital angular momentum will have zeros on the negative energy axis. The higher the angular momentum, the closer they will lie to threshold. Thus we do not expect to see an upturn when the capture occurs from a high-angular-momentum state.

IV. COMPARISON WITH CLUSTER MODELS

The other class of models which has been used in the analysis of the data is composed of the cluster models [6,13,25–27]. These generator-coordinate models (GCM's) calculate the S factor microscopically and incorporate many-body effects which are not included explicitly in the simpler one-body potential models. They predict the absolute magnitude as well as the energy dependence. However, the use of the more sophisticated models comes at a price: it is more difficult to discern the dominant physical effects and to understand the differences between the various calculations. Fortunately, the hard sphere model can be used to clarify these issues.

We compare the results of the hard sphere model calculation, with $r_c = 0$ fm, with the GCM calculations of Descouvemont and Baye (DB) [13] and the GCM calculations of
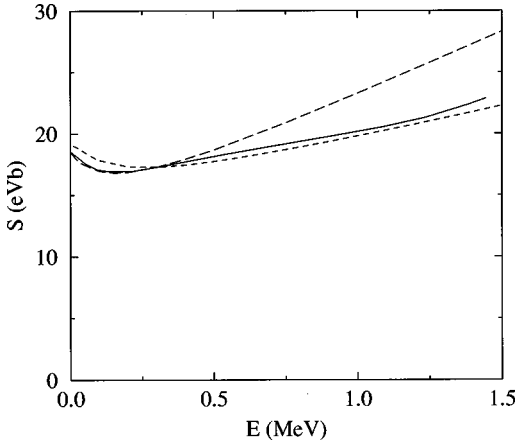
FIG. 7. The *S* factor as a function of energy for various models. The solid curve is the result of the DB GCM calculation (as quoted by Hammache *et al.* [4]). The short-dashed curve is the result of the C2B model calculation, while the long-dashed curve is the hard-sphere model result with $r_c=0$ fm. The curves are normalized to agree at 0.3 MeV.

Csótó *et al.* [25] (denoted as C2B) in Fig. 7. The hard sphere, DB, and C2B results are displayed by the long-dashed, solid, and short-dashed lines, respectively. In the GCM calculation, C2B, the effect of intercluster antisymmetrization, leading to effective eight-body wave functions, has not been included. All results have been normalized to agree at 300 keV. Above this energy, the two GCM results agree with each other, while below the result of DB is consistent with that of the $r_c=0$ fm hard sphere model. However, the C2B calculation is consistent with the hard sphere model result with $r_c=2.4$ fm, as shown in Fig. 8. There, that result is displayed by the solid line while the hard sphere model result is displayed by the dot-dashed line. We show by the dotted line the calculation, by Csótó, which includes antisymmetrization [26]. This calculation will hereafter be referred to as the C8B model. While this calculation shows the same energy dependence as the C2B result near threshold, there is a marked change above 500 keV.

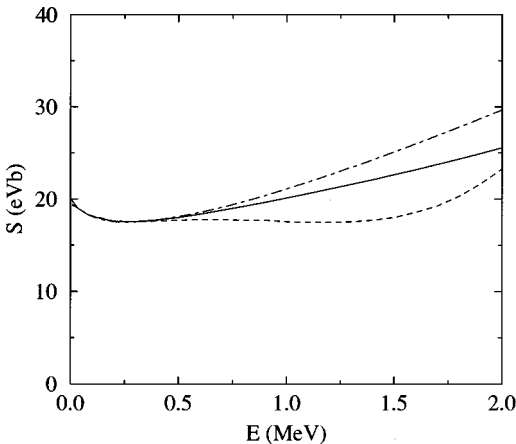The differences between the C2B and C8B GCM calcu-

FIG. 8. The *S* factor as a function of energy for various models. The C2B and C8B GCM model results are displayed by the solid and dashed lines, respectively. The result of the $r_c=2.4$ fm hard sphere calculation is shown by the dot-dashed line.

lations, manifest at higher energies, have their source in both the *s*- and *d*-wave contributions [28]. The difference in the *s*-wave calculations is relatively small and consistent with the expected model dependence due to the different short-range behavior. The effect is much more dramatic for the *d* waves; the contribution from three of the *d*-wave channels goes to zero [28] at approximately 1.5 MeV. That behavior is inconsistent with the very small effects of nuclear distortion in the *d*-wave component observed in the one-body models.

Outside the range of the nuclear force the wave functions, and hence the matrix element, are determined by the properties of the Coulomb force, the asymptotic strength, and the phase shift. As the two calculations of Csótó have the same phase shift [26,28] the only difference must be at short distances, less than ~3 fm. At 1.5 MeV, the integrand peaks at 14.5 fm, as determined by the Coulomb properties and the phase shift. Therefore the antisymmetrization, being the only difference between the two- and eight-body models, must make the integrand very large at small radii. That is possible if there is a resonance and, in that case, the whole *d*-wave contribution may indeed vanish. This may be simulated in the Woods-Saxon model by increasing the depth of the potential. However, a resonance would have a very pronounced effect on the phase shift, and there is no indication of a resonance in the *d*-wave component. It is also inconsistent with the statement that the two calculations of Csótó have the same phase shift.

We note that in the potential models antisymmetrization is not a problem. One can construct a fully antisymmetric eight-body wave function for the ^{7}Be-*p* system by taking a Slater determinant of the bound states wave functions and the scattering wave function. Orthogonality is assured between the wave functions when they are calculated with the same potential, and the Slater determinant is trivially constructed. As the transition operator is one-body in our model only the incoming proton is involved in the interaction with the mean field defined by the ^{7}Be nucleus as a whole. Antisymmetrization then becomes a problem only when one ventures beyond the potential model and has wave functions that are not orthogonal by construction.

V. COMPARISONS WITH THE DATA

The discussions in the previous sections have concentrated on theoretical aspects of the low-energy behavior of the *S* factor. We now turn to the data to determine the normalization and a meaningful value of the *S* factor at astrophysical energies. When discussing the ^{7}Be$(p,\gamma)^8$B *S*-factor data, it is important to consider resonant capture. The main resonance in the reaction at low energies is the *M*1 resonance at 0.637 MeV for the capture to the 0.774 MeV state in ^{8}B [16]. There is another, much weaker and wider, resonance in the cross section at 2.183 MeV corresponding to the 2.32 MeV state in ^{8}B [16]. We limit our comparisons to *E* <1.5 MeV, to avoid the influence of this wider state, and assume the resonance at 0.637 MeV to be of Breit-Wigner form.

There have been seven measurements of the ^{7}Be$(p,\gamma)^8$B *S* factor. Two of these [29,30] have large error bars and data points at only a limited number of energies, two and one, respectively. This limits their usefulness and

TABLE V. Values of $S(20)$ in eV b extracted from the various experimental data sets with different models. For each data set, except Vaughn *et al.*, we have two columns showing the extracted value of $S(20)$ using data up to 400 keV and 1.5 MeV, respectively. The last two columns give the weighted average of the S factor obtained from the data sets of Vaughn *et al.*, Filippone *et al.*, and Hammache *et al.* The last row is the standard deviation errors on the value of the S factor including both statistical and normalization errors.

Model	Kavanagh *et al.*		Vaughn *et al.*	Filippone *et al.*		Hammache *et al.*		Average	
$r_c = 2.4$ fm	24.3	25.1	18.1	19.3	18.7	19.5	18.7	19.4	18.6
B1	24.1	24.7	17.7	19.1	18.4	19.3	18.4	19.2	18.3
C2B	24.0	25.2	19.1	19.1	18.9	19.3	19.2	19.2	19.1
C8B	24.0	26.1	22.7	19.2	20.0	19.4	20.9	19.3	21.0
$r_c = 1.0$ fm	23.3	23.3	16.0	18.5	17.1	18.5	16.9	18.5	16.9
B2	23.3	23.5	16.6	18.5	17.3	18.4	17.2	18.4	17.2
DB	23.2	23.9	17.9	18.4	17.8	18.3	18.0	18.3	18.0
σ	1.9	1.9	1.5	1.6	1.5	1.4	0.9	1.1	0.8

we will not consider them further. The remaining five measurements fall into two basic classes. The first is comprised of the data of Kavanagh *et al.* [31] and of Parker [32]. Those data are on average ~30% greater in magnitude than the data of Filippone *et al.* [2], Vaughn *et al.* [3], and the most recent measurement of Hammache *et al.* [4]. The areal density of the ^{7}Be target is frequently determined by measuring the ^{7}Li(d,p) cross section σ_{dp} and normalizing the data to the known value. We follow the recommendation of [24] and take $\sigma_{dp} = 147 \pm 11$ mb for all the data sets. Strieder *et al.* [33] quote smaller errors, $\sigma_{dp} = 146 \pm 5$, while a recent measurement [34] gives $\sigma_{dp} = 155 \pm 8$ mb. The use of the different values for this normalizing reaction shifts the results only slightly. The measurements of Filippone *et al.* [2] and of Hammache *et al.* [4] also determined the density by direct measure of the β-delayed γ rays, and found very good agreement between the two normalization methods.

To extract a reliable value of the S factor at astrophysical energies we must carefully consider the experimental errors. Some of the errors are common between different data sets: for example, the value of σ_{dp} used in the normalization. Also in fitting individual data sets errors common to all the points must be handled separately. Thus we fit each data set separately using just the relative errors. The sets used are Kavanagh *et al.* [31], Vaughn *et al.* [3], Filippone *et al.* [2], and the two data sets of Hammache *et al.* [4]. That measurement reports two data sets from runs taken in different years with different normalization errors. Hence, the two data sets of Hammache *et al.* are fit separately using just the relative errors and combined using both relative and absolute errors. In averaging the values of $S(20)$ obtained from the fits to the data of Vaughn *et al.* and Filippone *et al.* we have taken into account the common error due to the uncertainty in σ_{dp} used for the normalization.

The resonance at 0.637 MeV was fit with the Breit-Wigner form. In comparisons to the data of Filippone *et al.* [2] and Kavanagh *et al.* [31] the parameters of the Breit-Wigner were determined by the fit to the data. In fitting the data of Vaughn *et al.* [3] and Hammache *et al.* [4] the resonance parameters were taken from the fit to the data of Filippone *et al.* Leaving out the resonance in the fit of the data of Hammache *et al.* raises the result by 2–3 %.

The values of $S(20)$ determined as a result of the fits to the data are shown in Table V for hard sphere ($r_c = 2.4$ and

1.0 fm), Woods-Saxon (B1 and B2), and GCM (DB, C2B, and C8B) models. For each model two fits are shown: the left column for each data set is the result obtained by fitting the data below 400 keV, while the right column is the result obtained by fitting up to 1.5 MeV. As the data of Vaughn *et al.* do not extend below 400 keV only the result of fitting to the higher energy is presented in that case. The final column lists the result of the average of the fits to the data of Vaughn *et al.*, Filippone *et al.*, and Hammache *et al.* The ideograms [35] for the B2, DB, C2B, and C8B results are displayed in Fig. 9 from top to bottom in the order listed. Therein, the results obtained from fitting the data of Filippone *et al.*, Vaughn *et al.*, and Hammache *et al.* below 1.5 MeV are displayed by the short-dashed, dot-dashed, and long-dashed lines, respectively. The solid line is the sum of all four Gaussian distributions; the peak at ~25 eV b was obtained from the data set of Kavanagh *et al.* As indicated by the disparity in the absolute magnitude, the results obtained from the data of Kavanagh *et al.* are consistently much
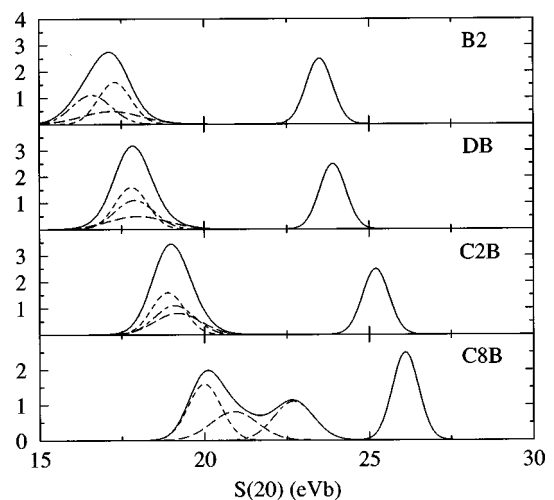

FIG. 9. Ideogram [35] for the S factor at 20 keV. The calculations are denoted by B2, DB, C2B, and C8B as defined in the text. The results obtained from the data of Filippone *et al.*, Vaughn *et al.*, and Hammache *et al.* are displayed by the short-dashed, dot-dashed, and long-dashed lines, respectively. The solid line is the sum of the contributions. The isolated peak at higher S values is from Kavanagh *et al.* [31].
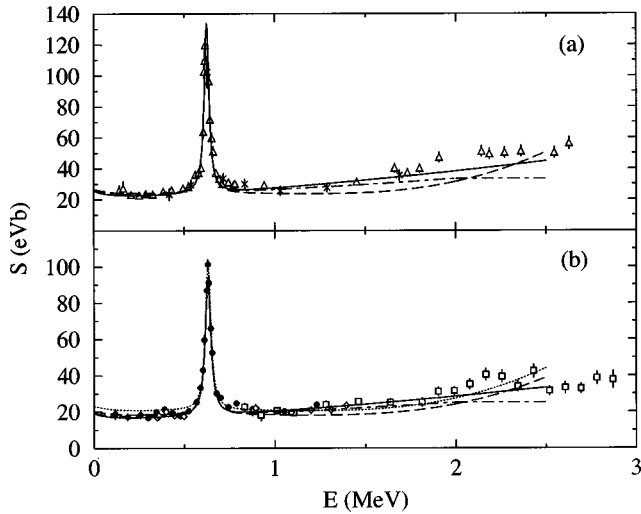
FIG. 10. The theoretical S factor as function of energy compared to the experimental data. In (a) we present the data of Kavanagh *et al.* [31] while in (b) we show the data of Vaughn *et al.* [3], Filippone *et al.* [2], and Hammache *et al.* [4]. In each figure, the solid line shows the B1 model result, while the dot-dashed and dashed curves are the results of the C2B and C8B calculations, respectively. In (b) the fits are to the data of Filippone *et al.*, with the exception of the dotted curve in (b) which is a fit to the data of Vaugh *et al.* using the C8B calculation. All the fits are to the 0–1.5 MeV energy range.

higher than those obtained from the other data sets. Hence it was not included in the average given in Table V.

The best consistency in the values of $S(20)$ among the data sets, excluding the data of Kavanagh *et al.*, is found with the fits using the C2B and DB models. The high quality of the fit to the data using the B1 and C2B models can be seen in Figs. 10 and 11. The quality of fit using the DB model is similar and is not shown. Note that the values obtained from the DB calculation are consistently lower than the C2B values by 3–6 %. Our DB result agrees with that quoted by Hammache *et al.* [4] who also used this calculation in their extrapolation. The GCM model calculation of Johnson *et al.* [6] has a very similar energy dependence to the DB calculation and would give similar results in a fit. The low values of $S(20)$ obtained with these models, compared to the C2B and C8B models, is a consequence of the energy dependence near threshold. As was shown in Fig. 7, the DB model calculation agrees with the hard sphere model for $r_c = 0$ fm in the low-energy region. The B2 Woods-Saxon model fit looks equally good but the extrapolated value of the S factor depends on the energy range used in the fit. The value drops by 5% for the larger energy range.
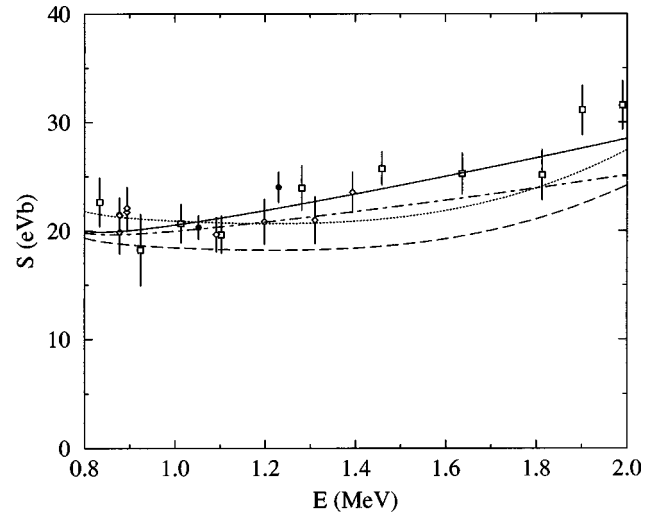
FIG. 11. Expanded view of the S factor as function of energy. This is an expanded view of Fig. 10(b) using the same conventions for the curves and data points.

The values of $S(20)$ obtained from fitting the C8B model to the data sets show much more dispersion than any of the other results, varying with both the energy range and data set used. The latter variation is clearly seen in the C8B ideogram, Fig. 9. This is reflected in Figs. 10 and 11, where the C8B calculation has the wrong energy dependence when compared to *any given data set*. While the data suggests a steady increase in the S factor above 1 MeV, the C8B result is relatively flat in the 1–2 MeV range and then shows a sharp increase above 2 MeV. This disagreement with the data must be understood before using this model to extrapolate the data to threshold.

In Table VI we show the χ^2 per degree of freedom for individual data sets for four different models. Only data below 1.5 MeV have been included in the fit. Each data set has a common normalization error which is not included in the calculation of χ^2. For the data of Hammache *et al.* [4] we fit only the 1996 data. The higher value of χ^2 per degree of freedom for the data of Kavanagh *et al.* [31] is due to three points on the lower side of the resonance peak; the fitting ignores any relative error in the energy calibration. For the other three data sets the χ^2 per degree of freedom is of order 1 except for the C8B results for which it is consistently higher. This reflects the incorrect energy dependence of the C8B model noted in the previous paragraph.

We may now discuss in more detail Fig. 1, where two extreme fits to the nonresonant part of the data are shown. The first is the naive straight line fit while the other is the hard sphere model result with $r_c = 4.1$ fm. These two results

TABLE VI. The χ^2 per degree of freedom for fits to individual data sets. Each fit is to a data set with common normalization errors and only the relatives errors are included. Only data below 1.5 MeV have been included in the fits.

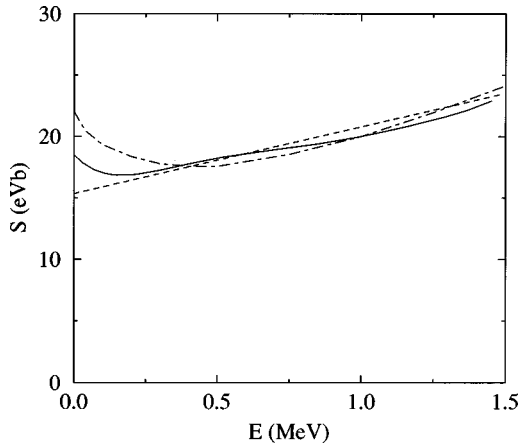| Model	Kavanagh *et al.*	Vaughn *et al.*	Filippone *et al.*	Hammache *et al.* 96
B1	2.5	0.6	1.0	0.8
C2B	2.6	0.9	1.0	0.9
C8B	3.7	1.6	1.8	2.7
DB	2.4	0.7	1.0	0.8

FIG. 12. The S factor as function of energy. The result of the DB calculation, the straight line fit from Fig. 1, and the $r_c = 4.1$ fm model calculation are displayed by the solid, dashed, and dot-dashed lines, respectively.

are compared to the DB GCM calculation in Fig 12. The resonant contribution has been removed from all the curves. All three results are in reasonable agreement with each other in most of the energy region where data exist, $E > 0.1$ MeV, hence the equally good fits. However, only the DB calculation contains the correct physics at low energy. The straight line fit does not contain any contribution from the pole term and hence no upturn, while the upturn in the $r_c = 4.1$ fm hard sphere model calculation is far too severe. Also, the curvature in that hard sphere model result is not seen in the GCM model calculations in the region of the data.

We can improve on the straight line fit by replacing the constant term with $\{0.0408/(0.1375 + E) + 0.7033\}$ from the rational approximation, Eq. (11). Since the ratio of the pole to constant term is fixed in an almost model-independent manner and the pole term, by itself, is poorly determined by the data, it makes little sense to fit these two terms separately. This leads to the form

$$S(E) = S(0)\left[\left(\frac{0.0408}{0.1375 + E} + 0.7033\right) + c'E\right], \quad (12)$$

where $S(0)$ and c' are fit parameters and E is in MeV. Using this form and a Breit-Wigner resonance we fit the data up to 1.5 MeV. The resulting fit $[S(0) = 18.5$ eV b and $c' = 0.351$ MeV$^{-1}]$ is as good as that with the straight line but the value of $S(20)$ is now 18.0 ± 0.9 eV b. This is in agreement with the DB results when fit over the same energy range. The parameter c', determined by the fit, is also close to that obtained from the B2 potential model and corresponds to a low value of r_c (see Table III).

VI. CONCLUSIONS

We have explored the energy dependence of the $^7\text{Be}(p,\gamma)^8\text{B}$ reaction and have constructed a simple model to illustrate the dominant physics. For energies $E < 0.4$ MeV, the S factor is dominated by a pole arising from the influence of the subthreshold ^8B ground state. The behavior of the S factor near threshold is determined by three parameters: the location and residue of the pole, and the effective hard

sphere radius. The location of the pole is set by the binding energy of the valence proton in ^8B, while the residue is proportional to the normalization of the S factor. The hard sphere radius simulates the effect of the nuclear distortion, and changes the slope of the S factor. The low-energy behavior of the models considered in this paper can be reproduced with r_c in the range 0–3 fm. If we restrict the comparison to models that fit the elastic scattering of neutrons from ^7Li, a value of 1 fm is preferred. The S-factor data do not distinguish between the results obtained with these values. While some models at low energy are consistent with a hard sphere model of $r_c = 0$ fm, suggesting no nuclear distortion at threshold, this is not of major concern: the preferred value of 1 fm is suitably well inside the nucleus so that the influence of nuclear distortion for what is, in effect, a surface capture is minimal. The range of r_c from 0 to 3 fm introduces an error of about 5% in the extrapolations even when only data below 400 keV are used. Restricting ourselves to models consistent with the elastic neutron ^7Li scattering data reduces this uncertainty to about 1%. Thus from fitting the energy range of 0–400 keV we have $S(20) = 18.4 \pm 1.0 \pm 0.2$ eV b or, equivalently, $S(0) = 19.0 \pm 1.0 \pm 0.2$ eV b, where the first error is experimental and the second is from model dependences in the fit.

As the energy increases beyond 400 keV the model dependences and, hence, uncertainties also increase. Yet even at the somewhat higher energy region $E < 2$ MeV the simple model gives indications of how large model effects might be. For example, the effect of nuclear distortion in the d-wave component of the S factor is at most 2% even for $E \sim 1.5$ MeV, as the scattering wave barely penetrates into the region where the nuclear forces are strong. Together with the comparison with existing data, this casts doubt on the eight-body model result of Csótó.

Of the models considered here, the DB and C2B GCM calculations have the least variation of the extracted $S(20)$ with the energy range fit, suggesting they do have a more accurate description of the physics in the higher-energy range. However, the GCM calculations predict the magnitude of $S(20)$ to be much higher than that we extract from the recent experimental data. As with the fit to the lower-energy range we restrict ourselves to models that are consistent with the neutron ^7Li elastic scattering data. Elastic p-^7Be scattering data would be useful in confirming the conclusions drawn from the elastic n-^7Li scattering data.

Neither data nor theoretical considerations are sufficiently refined to completely rule out the Woods-Saxon models. The value of $S(20)$ differs by 5% depending on whether the GCM or the Woods-Saxon model is used for the extrapolation. Taking this as an indication of the error for the fit in the energy range $E < 1.5$ MeV we then obtain $S(20) = 17.6 \pm 0.7 \pm 0.4$ eV b and $S(0) = 18.1 \pm 0.7 \pm 0.4$ eV b. The second error comes from the uncertainty (half the spread) in the choice of model used in the extrapolation. As the theoretical error here is not well understood we prefer the values of the S factor extracted from the more restricted energy range. Phase shift information from proton ^7Be scattering in the 1 MeV region would reduce the theoretical uncertainty from the fit over the larger energy range.

ACKNOWLEDGMENTS

[1] J. N. Bahcall and M. Pinsonneault, Rev. Mod. Phys. **67**, 781 (1992); J. N. Bahcall, S. Basu, and M. H. Pinsonneault, Phys. Lett. B **433**, 1 (1998).

[2] B. W. Filippone *et al.*, Phys. Rev. Lett. **50**, 412 (1983); B. W. Filippone *et al.*, Phys. Rev. C **28**, 2222 (1983).

[3] F. J. Vaughn *et al.*, Phys. Rev. C **2**, 167 (1970).

[4] F. Hammache *et al.*, Phys. Rev. Lett. **80**, 928 (1998).

[5] R. F. Christy and I. Duck, Nucl. Phys. **24**, 89 (1961).

[6] C. W. Johnson, E. Kolbe, S. E. Koonin, and K. Langanke, Astrophys. J. **392**, 320 (1992).

[7] F. C. Barker, Aust. J. Phys. **33**, 177 (1980).

[8] F. C. Barker, Phys. Rev. C **28**, 1407 (1983).

[9] F. C. Barker, Nucl. Phys. **A588**, 693 (1995).

[10] T. A. Tombrello, Nucl. Phys. **71**, 459 (1965).

[11] R. G. H. Robertson, Phys. Rev. C **7**, 543 (1973).

[12] K. H. Kim, M. H. Park, and B. T. Kim, Phys. Rev. C **35**, 363 (1987).

[13] P. Descouvemont and D. Baye, Nucl. Phys. **A567**, 341 (1994).

[14] F. M. Nunes, R. Crespo, and I. J. Thompson, Nucl. Phys. **A615**, 69 (1997); **A627**, 747 (1997); **A634**, 527 (1998).

[15] B. K. Jennings, S. Karataglidis, and T. D. Shoppa, Phys. Rev. C **58**, 579 (1998).

[16] F. Ajzenberg-Selove, Nucl. Phys. **A490**, 1 (1988).

[17] H. M. Xu, C. A. Gagliardi, R. E. Tribble, A. M. Mukhamed-zhanov, and N. K. Timofeyuk, Phys. Rev. Lett. **73**, 2027 (1994).

[18] I. Tanihata, H. Hamagaki, O. Hashimoto, Y. Shida, N. Yoshikawa, K. Sugimoto, O. Yamakawa, T. Kobayashi, and N. Takahashi, Phys. Rev. Lett. **55**, 2676 (1985).

[19] L. Koester, K. Knopf, and W. Waschkowski, Z. Phys. A **312**, 81 (1983).

[20] E. Vogt, Phys. Lett. B **389**, 637 (1996).

[21] R. D. Williams and S. E. Koonin, Phys. Rev. C **23**, 2773 (1981).

[22] *Handbook of Mathematical Functions*, edited by M. Abramowitz and I. A. Stegun, Natl. Bur. Stand. Appl. Math. Ser. No. 55 (U.S. GPO, Washington, D.C., 1965), p. 539, Eqs. (14.4.1) and (14.4.2).

[23] D. Baye, P. Descouvemont, and M. Hesse, Phys. Rev. C **58**, 545 (1998).

[24] E. Adelberger *et al.*, Rev. Mod. Phys. **70**, 1265 (1998).

[25] A. Csótó, K. Langanke, S. E. Koonin, and T. D. Shoppa, Phys. Rev. C **52**, 1130 (1995).

[26] A. Csótó, Phys. Lett. B **394**, 247 (1997).

[27] P. Descouvemont and D. Baye, Nucl. Phys. **A487**, 420 (1988).

[28] A. Csótó (private communication).

[29] R. W. Kavanagh, Nucl. Phys. **15**, 411 (1960).

[30] C. Wiezorek, H. Kräwinkel, R. Santo, and K. Wallek, Z. Phys. A **282**, 121 (1977).

[31] R. W. Kavanagh, T. A. Tombrello, J. M. Mosher, and D. R. Goosman, Bull. Am. Phys. Soc. **14**, 1209 (1969).

[32] P. D. Parker, Phys. Rev. **150**, 851 (1966).

[33] F. Strieder *et al.*, Z. Phys. A **355**, 209 (1996).

[34] L. Weissman, C. Broude, G. Goldring, R. Hadar, M. Haas, F. Schwamm, and T. Shannan, Nucl. Phys. **A630**, 678 (1998).

[35] Particle Data Group, Phys. Lett. **170B**, 1 (1986).